ACS APPLIED MATERIALS & INTERFACES

Research Article

www.acsami.org

Limitations of $Cs_3Bi_2I_9$ as Lead-Free Photovoltaic Absorber Materials

Biplab Ghosh,[†,∥] Bo Wu,[‡] Hemant Kumar Mulmudi,[§] Claude Guet,[†,⊥] Klaus Weber,[§] Tze Chien Sum,[‡] Subodh Mhaisalkar,[†,⊥] and Nripan Mathews*[,†,⊥]

[†]Energy Research Institute @ Nanyang Technological University (ERI@N), 637553, Singapore

[‡]Division of Physics and Applied Physics, School of Physical and Mathematical Sciences, Nanyang Technological University, 637371, Singapore

[§]Centre for Sustainable Energy Systems, Research School of Engineering, The Australian National University, Canberra 2601, Australia

[∥]Interdisciplinary Graduate School, Nanyang Technological University, 639798, Singapore

[⊥]School of Materials Science and Engineering, Nanyang Technological University, 639977, Singapore

Supporting Information

ABSTRACT: Lead (Pb) halide perovskites have attracted tremendous attention in recent years because of their rich optoelectronic properties, which have resulted in more than 22% power conversion efficient photovoltaics (PVs). Nevertheless, Pb-metal toxicity remains a huge hurdle for extensive applications of these compounds. Thus, alternative compounds with similar optoelectronic properties need to be developed. Bismuth possesses electronic structure similar to that of lead with the presence of ns^2 electrons that exhibit rich structural variety as well as interesting optical and electronic properties. Herein, we critically assess $Cs_3Bi_2I_9$ as a candidate for thin-film solar cell absorber. Despite a reasonable optical band gap (~2 eV) and absorption coefficient, the power conversion efficiency of the $Cs_3Bi_2I_9$ mesoscopic solar cells was found to be severely lacking, limited by the poor photocurrent density. The efficiency of the $Cs_3Bi_2I_9$ solar cell can be slightly improved by changing the stoichiometry of the precursor solutions, which is most probably due to the reduction in nonradiative defects as evident from our single-crystal photoluminescence spectroscopy. However, detailed investigations on pristine $Cs_3Bi_2I_9$ reveal that zero-dimensional molecular crystal structure remains one of the main bottlenecks in achieving high performance. On the basis of our comprehensive studies, we have proposed that a continuous network of three-dimensional crystal structure should be another major criterion in addition to proper band gap and suitable optical properties of the future PV compounds.

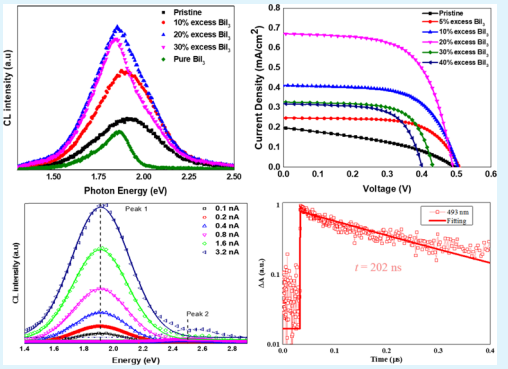

KEYWORDS: *photovoltaics, lead-free, perovskite solar cell, bismuth-based perovskite, cathodoluminescence, $Cs_3Bi_2I_9$*

INTRODUCTION

In the search for cheap and earth-abundant semiconductors for photovoltaics (PVs), lead-based halide perovskites have recently outperformed other new technologies.[1−4] The efficiency of Pb-based halide perovskite solar cells has increased from mere ~4% to more than 22% (certified) within half a decade. Nevertheless, major challenges such as lead toxicity and atmospheric stability are still huge hurdles for the extensive application of Pb-based halide perovskites. These problems can be addressed by utilizing nontoxic metal cations that can replace lead and possibly provide better atmospheric stability. The most suitable replacement would be by an equivalent ns^2 valence ion such as Sn^{2+} or Ge^{2+}. However, recent studies indicate that both elements either suffer from lower stability than lead or have similar toxicity.[5−8] In a similar way, substitution by an isoelectronic Bi^{3+} can be another good alternative to replace Pb^{2+}. Lehner et al.[9] examined several Bi-based inorganic ternary halides ($(K/Rb/Cs)_3Bi_2I_9$) and found that the effect of these cations on the band gap is negligible with an optical band gap of ~2 eV, which would translate to a theoretical efficiency of 22.6%.[10,11] Early experimental results from Park et al.[12] reported $MA_3Bi_2I_9$- (MA = CH_3NH_3) and $Cs_3Bi_2I_9$-based PVs with power conversion efficiencies of 0.12 and ~1%, respectively, in mesoscopic solar cell configurations. Shortly after, several research articles have been published on Bi-based ternary iodides as perovskite solar cell absorber materials with poor power conversion efficiencies which limit the practical use of Bi-based solar cells.[13−15] Herein, we have fabricated $Cs_3Bi_2I_9$-based mesoscopic solar cells which confirm the poor power conversion efficiencies of this material system. Noting the effects of precursor stoichiometry on the efficiency values, we have chosen to focus on the underlying reasons

Received: September 27, 2017
Accepted: January 17, 2018
Published: January 17, 2018

DOI: 10.1021/acsami.7b14735
ACS Appl. Mater. Interfaces XXXX, XXX, XXX−XXX

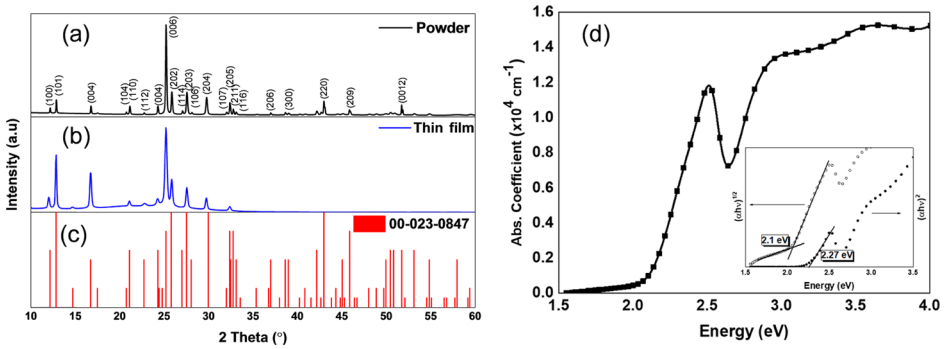

Figure 1. (a) Grazing-angle XRD pattern of thin films, (b) powder XRD pattern, and (c) reference (00-023-0847) XRD pattern of $Cs_3Bi_2I_9$; (d) absorption coefficient spectrum at different photon energies (inset: Tauc plot of UV−vis absorbance spectrum of $Cs_3Bi_2I_9$ thin films).

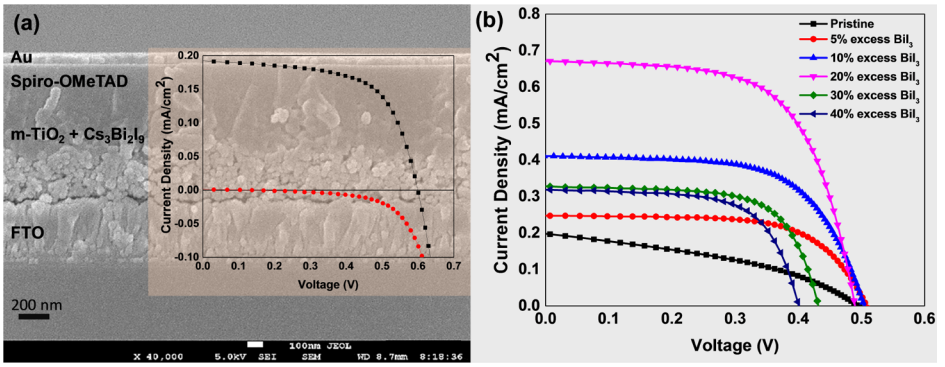

Figure 2. (a) $Cs_3Bi_2I_9$-based mesoscopic solar cell cross section with Spiro-OMeTAD as hole transport materials ($J-V$ curve of the solar cell in dark and 1 sun conditions) and (b) $J-V$ characteristics of $Cs_3Bi_2I_9$-based mesoscopic solar cell with different precursor solution stoichiometries.

behind the low efficiency of the Bi-based ternary halide system by exploring the optoelectronic properties of $Cs_3Bi_2I_9$.

RESULTS AND DISCUSSION

Physical Characterization. To evaluate $Cs_3Bi_2I_9$ for PV applications, it is utmost critical to obtain the pure phase compound during synthesis. The thin films of $Cs_3Bi_2I_9$ were prepared by solution processing via spin-coating ~~equimolar~~ CsI and BiI_3 dissolved in anhydrous *N*,*N*-dimethylformamide (DMF), followed by annealing at 100 °C. Single crystals of $Cs_3Bi_2I_9$ were grown by the antisolvent method. The grazing-angle diffraction patterns of the thin films and powder X-ray diffraction (XRD) patterns of single crystals are shown in Figure 1a,b, respectively. The reference pattern of $Cs_3Bi_2I_9$ was also included (Figure 1c) to illustrate the absence of any impurity phases such as BiI_3 or CsI. As illustrated in Figure 1a, although the positions of the reflections perfectly match the reference pattern, one can observe that the intensity of the {00*l*} reflections is much higher for thin films which can be attributed to the preferential orientation of the grains. This is confirmed by the scanning electron microscopy (SEM) image of the thin films which shows the presence of thin hexagonal platelets with needlelike protrusion (Figure S1). In addition, the higher angle reflections in grazing-angle XRD patterns of the thin films are completely missing which may be due to the thickness. On the other hand, the powder XRD patterns from crushed single crystals do not suffer from prominent preferential orientations, and the high-angle reflections are well-matched with the reference patterns.

Unlike conventional semiconductors, $Cs_3Bi_2I_9$ exhibits a strong excitonic behavior at room temperature as revealed by ultraviolet−visible (UV−vis) absorption measurements shown in Figure 1d. Although the sharp excitonic resonance signature is common for low-dimensional perovskite materials at room temperature, it is inseparable from the continuous absorption edge for three-dimensional (3D) perovskites. For $Cs_3Bi_2I_9$, the excitonic absorption peak at ~485 nm (2.56 eV) is usually related with the strong quantum confinement effect because of the 0D nature of $[Bi_2I_9]^{3-}$ bioctahedra.[16,17] Using Tauc plot (Figure 1d inset), we estimated the indirect optical band gap to be ~2.1 eV. Although, the band gap is indirect in nature, it is reasonably suitable for PV applications with other low band gap absorber materials in tandem solar cell configurations. The measured optical absorption coefficient of ~1 × 10^4 cm^{-1} at 450 nm for $Cs_3Bi_2I_9$ thin films is also reasonable for such high and indirect band gap materials but is at least one order smaller than $MAPbI_3$ thin films.[18] The observed exponential absorption tail below the optical band gap can be associated with the intrinsic disorder in the semiconducting materials. Both the exponential tail below band gap and strong excitonic binding energy are detrimental for PV applications because of lesser number of available free carriers.

Photovoltaic Performance. The PV performances of $Cs_3Bi_2I_9$ as an absorber layer were investigated in mesoscopic solar cell architecture, following the initial report by Park et al.[12] Thin films of $Cs_3Bi_2I_9$ were deposited onto mesoporous TiO_2 films inside the Ar-filled glovebox and annealed at 100 °C for 15 min. The annealing time was kept lower than the previous report as we find negligible effect on the device performances. After cooling down, an HTM layer of Spiro-OMeTAD was spin-coated onto the absorber layer, followed by thermal evaporation of Au contacts. Detailed procedures for device fabrication can be found in the Experimental Section.

DOI: 10.1021/acsami.7b14735
ACS Appl. Mater. Interfaces XXXX, XXX, XXX−XXX

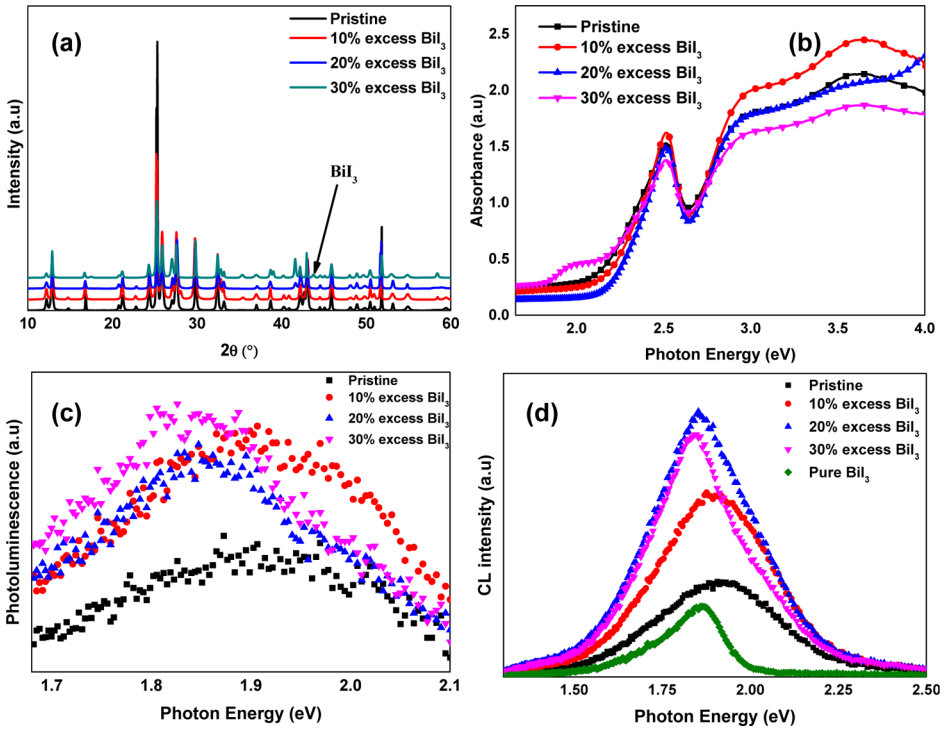

Figure 3. (a) Powder XRD patterns of different stoichiometric compositions. Data are shifted along *Y*-axis for easier comparison. (b) UV–vis, (c) PL, and (d) CL spectra (I_b = 0.2 nA) of the same samples as in (a). CL spectrum of BiI_3 was included for comparison.

The device cross section and the *J*–*V* characteristics of our champion cell, which yields a power conversion efficiency (PCE) of ~0.07%, are shown in Figure 2a. Besides a solitary publication which reported a PCE value close to 1%, recent follow-up reports only attained 0.02% PCE with $Cs_3Bi_2I_9$.[19] Hence, the performances of our devices are comparable to more recent reported values. In addition to the mesoscopic architecture, we have also fabricated planar and inverted structures, utilized antisolvent treatments as well as various hole-transporting materials to ascertain the performance of $Cs_3Bi_2I_9$-based solar cells (details of the solar cells are provided in Note 1 of the Supporting Information). However, PCEs remained low, limited by poor photocurrent density. The results of such investigations are included in the Supporting Information (Figures S2 and S3). As the $Cs_3Bi_2I_9$-based solar cells are limited by poor photocurrent density, we took inspiration from a similar problem faced earlier on Sn-based perovskite. Kumar et al.[20] had illustrated that the photocurrent density of $CsSnI_3$ can be improved by excess Sn^{2+} cations. Pb-based perovskites are also showed to have improved performance with excess PbI_2.[21,22] In a similar manner, we have fabricated mesoscopic solar cells with different stoichiometric precursor solutions. With increasing BiI_3 concentration in the precursor solutions, we found that there is a sharp increase in the photocurrent density (Figure 2b). The best PV performance was observed with 20% excess BiI_3 addition to stoichiometric $Cs_3Bi_2I_9$ with PV parameters: V_{OC} = 0.49 V, J_{SC} = 0.67 mA·cm^{-2}, and fill factor = 63.6%, which resulted 0.21% PCE. The current density of the solar cell is confirmed by the integrated current density obtained from the incident current-to-photon conversion efficiency (IPCE) measurement (Figure S5). However, with further increase in BiI_3 concentration or increase in CsI concentration, the PCE of the solar cell devices decreases. The *J*–*V* parameters of the $Cs_3Bi_2I_9$-based solar cell with different stoichiometric precursor solutions are provided in Table S1.

To illustrate the role of excess BiI_3 in the solar cell devices, we characterized the thin films using XRD, optical absorption, and luminescence spectroscopy. Figure 3a shows the powder XRD patterns of $Cs_3Bi_2I_9$ with varying excess BiI_3 concentration. Powders of different stoichiometric concentrations were collected after the precursor solution was drop-casted on the glass substrate, followed by annealing in a vacuum oven at 100 °C for 24 h. Interestingly, there is no noticeable change in peak positions or the peak intensities of the reflections till 20% excess BiI_3 addition, signifying no change in the crystal structure. Further increase in BiI_3 in the precursor solution results in the formation of secondary phase of BiI_3. This observation is also confirmed by the presence of another optical absorption peak near 1.7 eV for 30% excess BiI_3 (Figure 3b). However, 10 and 20% excess BiI_3 stoichiometric films show no indication of secondary phases from XRD patterns. Moreover, there is no apparent change in film morphology with different stoichiometries as shown in the SEM image of the thin films (Figure S6). Hence, the improvement of PV performance with small amount of excess BiI_3 addition can be correlated with the passivating intrinsic defects or structural disorder. We have earlier shown through first-principle calculations that defects are energetically favorable and create mid-band gap states in $Cs_3Bi_2I_9$.[23] To justify our hypothesis, we have further characterized the thin films prepared under different stoichiometric ratios using photoluminescence (PL) and cathodoluminescence (CL) spectroscopy. Both spectroscopic results indicate enhanced emission intensity with the addition of excess BiI_3, as illustrated in Figure 3c,d. However, as the photoluminescence quantum efficiencies (PLQEs) of the thin films are quite low and peaks are broad in nature, quantitative analysis using PL remains difficult. Nevertheless, the increase in

DOI: 10.1021/acsami.7b14735
ACS Appl. Mater. Interfaces XXXX, XXX, XXX–XXX

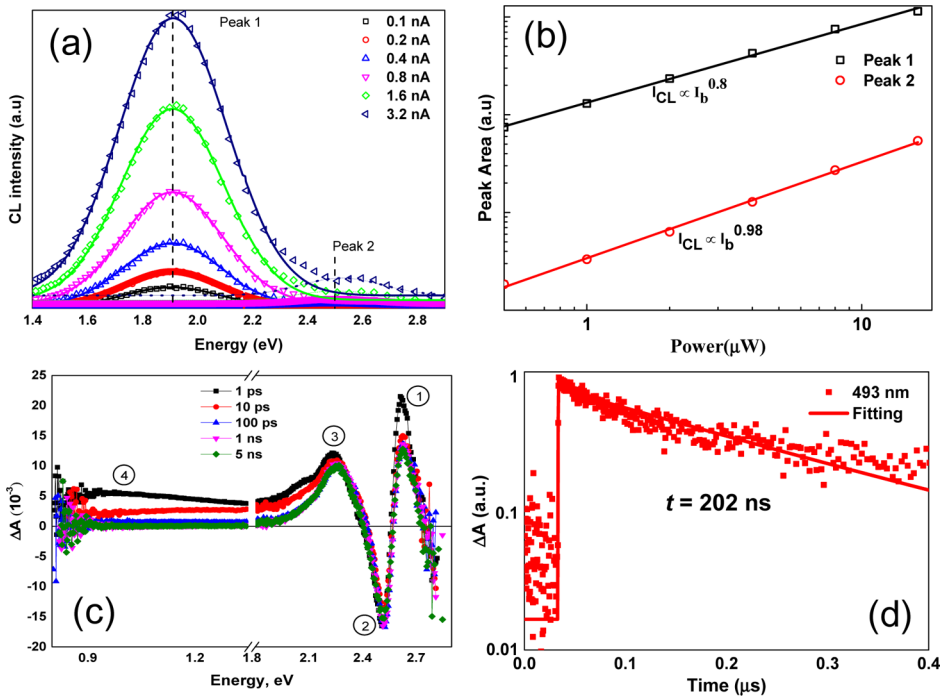

Figure 4. (a) Gaussian fitting of CL spectra of $Cs_3Bi_2I_9$ thin films at different electron beam currents (I_b), (b) power-law fits of CL peak area (see text for details) against different electron beam powers, (c) TA spectra of $Cs_3Bi_2I_9$ thin films for different time delays under 400 nm excitation, and (d) carrier decay dynamics of the same at 493 nm.

intensity can be correlated with passivation of nonradiative trap states that are inherently present in $Cs_3Bi_2I_9$. Moreover, similar results can also be observed with CL measurement. The small shift of the CL peak for higher BiI_3 addition can be associated with the formation of small BiI_3 after passivating the defects which is quite difficult to detect by conventional XRD at low concentration and become prominent at higher fraction as revealed by the XRD pattern of 30% excess BiI_3. Transient absorption (TA) spectroscopy also reveals similar carrier dynamics with different BiI_3 concentrations (Figure S9). Hence, excess BiI_3 is most probably going inside the trap states and the structural disorder that are present in $Cs_3Bi_2I_9$. Although the device performances are not promising for practical PVs, there is a clear indication of improvement of the materials as well as its properties that are important for optoelectronic applications.

Photophysical Characterization. As indicated, our results on the PV performance of $Cs_3Bi_2I_9$-based devices confirm the poor efficiencies noted in this material. This motivated us to extend our investigation to the photophysical properties of $Cs_3Bi_2I_9$ to unravel the origins of such low performances. PL spectroscopy is one of the most common techniques utilized to measure radiative recombination, which should be maximized for PV applications.[24] However, as an indirect band gap material, $Cs_3Bi_2I_9$ thin films do not exhibit a prominent PL spectrum, rather a broad and asymmetric luminescence peak (PLQE < $\sim 10^{-5}$, as illustrated in Figure S6) which is difficult to characterize. As solution-processed thin films often suffer from nonequilibrium defects, we have extended our PL studies to single crystals. As is evident from Figure S7, the single crystals exhibit a remarkably stronger emission peak centered around 1.86 eV as compared to that of thin films, which is possibly due to the increased optical path as well as reduced trap states for nonradiative recombination. The low PLQE from $Cs_3Bi_2I_9$ is expected as the radiative recombination of the indirect band edge only occurs when phonons are involved to conserve the momentum, which results in a very low quantum yield and broad spectrum. To verify this, we carried out transient PL spectroscopy of thin films as well as single crystals to determine the carrier lifetime. If the origin of the luminescence is from the indirect band edge, then the carriers that are located at the indirect band edge should exhibit long lifetime (vide infra). As illustrated in Figure S8, thin films show a biexponential decay with time constants of 5 ps (98%) and 73 ps (2%), whereas single crystals have a lifetime of ~160 ps which are much shorter as compared to the lifetime of indirect band-edge carriers. Hence, phonon-assisted multiple self-trapped exciton emission model seems more plausible for the broad emission from $Cs_3Bi_2I_9$ as reported recently by McCall et al.[25] from their low-temperature PL studies.

To further resolve the nature of the emission which was difficult to characterize because of low PLQE of the thin films, we have explored CL spectroscopy in which high-energy electron beam can provide better spatial resolution than conventional PL spectroscopy because of the order-of-magnitude higher carrier generations.[26] The typical CL spectra (Figure 4a) of $Cs_3Bi_2I_9$ thin films show two emission bands centered at 1.91 and 2.5 eV (represented as peak 1 and peak 2, respectively). The latter can be assigned to the direct exciton emission as the position corresponds well with the direct exciton absorption peak, which was absent in our room-temperature PL studies.[12,25] As a step further, we have extended our CL studies at varied excitation power (represented by the electron-beam current I_b) and analyzed using a simple power law model,[27] $I_{CL} \propto I_b^k$. The power-law fits as illustrated in Figure 4b reveal that the intensities of peak 2 and peak 1 display a linear and a sublinear relationship with the excitation power, respectively. The linear relationship between intensity and excitation for peak 2 confirms the free excitonic luminescence of $Cs_3Bi_2I_9$, which was too weak to be detected in typical PL

DOI: 10.1021/acsami.7b14735
ACS Appl. Mater. Interfaces XXXX, XXX, XXX−XXX

studies. The sublinear dependence of peak 1 on power is also consistent with the localized nature of the self-trapped excitons by extrinsic defects.[27−29] It can also be observed that in the whole range of excitation power, the shape and position of the peak remain unchanged (Figure 4a), which excludes the possibility of donor−acceptor-pair exciton formation.[30]

As the low PLQE limits the utility of PL spectroscopy, we have carried out TA spectroscopy analysis on thin films to elucidate the dynamics of the photoexcited carriers. As illustrated in Figure 4c, several features can be identified from the TA spectra under 400 nm excitation at different time delays: (2) a negative TA peak at around 2.52 eV (492 nm) ($\Delta A < 0$, $\Delta T/T > 0$); (1) and (3) two positive TA peaks at 2.62 eV (473 nm) and 2.23 eV (554 nm), respectively; and (4) a broad, feature-less photoinduced absorption (PIA) extending from visible to near-infrared (NIR) region. The negative peak corresponds well with the exciton peak shown in the steady-state absorption spectrum (Figure 1d); hence, we attribute it to the photobleach of the exciton peak after photoexcitation. The broad PIA extending from visible to NIR region shows an immediate subpicosecond rise after photoexcitation (within our system response), followed by a very fast decay (τ_1 = 4 ps, τ_2 = 68 ps). The spectrum feature, together with the immediate rise and fast decay, points that the broad PIA can be attributed to the absorption from the "hot carrier" located at the Γ valley (direct transition region) before relaxation to the indirect band edge (0.75 K Γ point).[23] Such fast decay within tens of picoseconds corresponds well with the intervalley relaxation mediated by carrier-phonon scattering.[31]

TA at exciton resonances can be induced by several mechanisms, such as phase-space filling, Coulombic screening, band gap renormalization, and so forth.[32] To elucidate the detailed mechanism, we analyzed the decay dynamics. The exciton bleaching peak decay contains multiple information: an initial fast decay corresponds to the hot carrier relaxation, followed by a slow rise and then an almost constant value within the 5 ns time window. Similar dynamics is also observed for the PIA at the blue side (1); the red side PIA (3) is slightly different, possibly because of the overlapping of the signals with the hot-carrier-induced absorption. In addition, the long residual as revealed by the nanosecond−microsecond TA in Figure 4d, shows a decay time constant of around 200 ns. The long-lived component cannot be attributed to the exciton recombination lifetime because that would imply strong PL and similar decay constants. The long-lived species is expected to originate from the relaxed carriers at the indirect band edge. Recombination via band-to-band transition is forbidden for the carriers located at the indirect band edge; therefore, they have a typical lifetime much longer than direct band gap materials. The dynamics of the exciton peak indicates that the dynamics does not originate from the exciton itself but instead is a result of the carriers-induced transmission change near the exciton resonance. Although phase-space filling usually only changes the oscillation strength of the excitons, Coulombic screening and band gap renormalization effects can result in exciton linewidth broadening and position shifts.[33] The bleaching near exciton resonance, together with two PIA bands lying on both sides of the bleaching peak, is a typical signature of exciton band broadening due to carrier-exciton scattering after photoexcitation.[31,34] In the initial time (∼10 ps), the broadening is mainly attributed to the nonrelaxed hot carriers; after that, the carriers that have gradually relaxed to the indirect band edge contribute to the scattering effects. Note that Scholz et al.[35] recently attributed a signal in $(MA)_3Bi_2I_9$ similar to the exciton Stark effect. Here in our $Cs_3Bi_2I_9$, the long-lived nature of the signal is because of the indirect band edge carriers, rather than due to excitons.

Through TA, we revealed the existence of large number of photoexcited carriers at the indirect band edge with a very long lifetime reaching 200 ns. Such long-lived carriers with even moderate carrier mobility should result in a high photocurrent, in striking contrast to our PV performance. We suspect that a very poor charge carrier mobility due to the discrete nature of the bioctahedra and subsequent bulk recombination would limit the extracted carrier density. Anisotropic carrier effective mass in $Cs_3Bi_2I_9$ as revealed in our simulation results also supports this hypothesis.[23] Photoexcited carriers in $Cs_3Bi_2I_9$ are relaxed and localized on the $[Bi_2I_9]^{3-}$ bioctahedra, which are surrounded by the isolating Cs^+ cations. This contrasts with 3D lead halide perovskites, in which the octahedras are connected and carriers are highly delocalized over many units.[36,37] In $Cs_3Bi_2I_9$, although photoexcited carriers can have a very long lifetime, they are unable to be extracted because of localization effects. This could also be a possible explanation for the poor performance of Cs_2SnI_6 which also offers high carrier lifetime but poor PV performance.[38] To resolve the bottleneck of charge carrier localizations, which is crucial to extract the free carriers for PV applications, the electronic dimensionality of lead-free perovskite compounds needs to be considered with more importance. For example, the PCE of the $Rb_3Sb_2I_9$-based perovskite solar cells improved drastically when the absorber layer is in two-dimensional phase as compared to the 0D dimer phase.[39]

Double perovskites such as $A_2M^+M^{3+}X_6$ in which partial substitution of Bi^{3+} with a cation of +1 charge state such as Ag^+ or In^+ could be another viable solution to improve the charge transport properties.[40] Double perovskites such as $Cs_2BiAgBr_6$ have recently been shown to have a better PV performance than $Cs_3Bi_2I_9$, although both compounds share similar optoelectronic properties.[41] The key difference between them is the crystal structure. Similarly, double perovskites such as $Cs_2InSbCl_6$ and $Cs_2InBiCl_6$ would also be exciting for PV applications.[40,42,43] In addition, total replacement of Cs with Ag also results in a 3D rudorffite crystal structure, which has been demonstrated to have much better performance than the Bi-based ternary halide system.[44] During the preparation of this article, Ni et al.[45] have experimentally validated the idea of charge carrier localization utilizing PL excitation spectra on $(CH_3NH_3)_3Bi_2I_9$. Hence, intrinsic defects, charge carrier localization, and anisotropic charge transfer remain major bottlenecks for a highly efficient $Cs_3Bi_2I_9$-based PV device.

CONCLUSIONS

In conclusion, we have systematically investigated the performances of nontoxic bismuth-based perovskite derivative, $Cs_3Bi_2I_9$ for applications in PVs. First, the poor power conversion efficiencies of $Cs_3Bi_2I_9$ were confirmed irrespective of the solar cell architecture. Second, the excess BiI_3 addition in the precursor solution was found to be beneficial in the PV performance because of suppression of intrinsic defects which is supported by the improved luminescence and PCE of the solar cells. In addition, TA spectroscopy has revealed the long carrier lifetimes of $Cs_3Bi_2I_9$ thin films. However, the PCE of the solar cells remains quite low for practical use in PV applications. Hence, on the basis of all of the above contrasting results, we conclude that poor charge transport may be the possible reason

DOI: 10.1021/acsami.7b14735
ACS Appl. Mater. Interfaces XXXX, XXX, XXX−XXX

for low performance of the $Cs_3Bi_2I_9$-based solar cell. Beyond our findings above, further enhancement in performance in the Bi-based solar cell can be expected by moving toward 3D crystal structure, which offers better charge transport properties than the molecular structure of $Cs_3Bi_2I_9$.

EXPERIMENTAL SECTION

The thin films of $Cs_3Bi_2I_9$ were deposited by codissolving BiI_3 and CsI (both are 99.999% pure and brought from Sigma-Aldrich) in DMF. In a typical experiment, 193.93 mg of CsI and 294.85 mg of BiI_3 were dissolved in 1 mL of anhydrous DMF and stirred at 70 °C for overnight. The single crystals of $Cs_3Bi_2I_9$ were produced by antisolvent diffusion crystallization method. Typically, 779.7 mg of CsI and 1179.38 mg of BiI_3 were dissolved in 10 mL of DMF, and the solution was filtered through 0.2 μm polytetrafluoroethylene syringe filter. The precursor solution containing vial was placed inside a beaker with toluene for few days to obtain micron-size single crystals.

Fluorine-doped tin oxide (FTO)-coated glass slides were first patterned by laser etching, followed by cleaning in soap solution, deionized water, and ethanol. A thin film of compact TiO_2 was deposited onto by spray pyrolysis of 600 μL of titanium diisopropoxide bis(acetylacetonate) solution (75% in 2-propanol) and 400 μL of acetylacetone, diluted in 2-propanol (1:7 v/v). The substrates were subsequently treated with $TiCl_4$ solution at 70 °C for 1 h, followed by annealing at 500 °C for 30 min. Mesoporous TiO_2 paste (Dyesol-30NRD) was diluted with ethanol (2:7 w/w) and spin-coated onto FTO substrates and annealed at 500 °C for 15 min. The mesoporous films were further treated with $TiCl_4$ solution similarly as mentioned before. Before spin-coating the precursor solution, the mesoporous substrates were plasma-cleaned using a UV-ozone plasma cleaner for 15 min. Around 40 μL of precursor solution was spread onto the substrate, followed by spin-coating at 2000 rpm for 30 s. The substrates were annealed afterward at 100 °C for 15 min on a hotplate. After deposition of $Cs_3Bi_2I_9$ films, suitable hole transport layer (HTM) such as SpiroOMeTAD (70 mg/mL in chlorobenzene) was spin-coated at 4000 rpm for 30 s. Around 80 nm Au contact electrode was deposited by thermal evaporation. The device area was defined by a metal mask with an aperture area of 0.2 cm^2.

XRD was carried out at room temperature to investigate the crystal structure and phases of the thin film and powder samples using a Bruker D8 ADVANCE Diffractometer (Bragg–Brentano geometry) with Cu Kα radiation (λ = 1.5418 Å). Field emission SEM (JEOL, JSM-7600F, operated at 5 kV) was used to characterize the surface and cross-sectional morphology of the thin films. To improve the resolution and reduce the charge collection on the surface, the samples were platinum-coated before analysis. UV–vis spectrophotometer (Shimadzu-3600) was used to characterize the absorption spectra of the thin film in the wavelength range of 300–800 nm at room temperature with integrated sphere attachment (ISR-3100) and 20 nm slit width. The CL measurements were performed on a FEI Verios SEM equipped with a Gatan MonoCL_4 Elite CL system. Samples were spin-coated onto a silicon substrate as described earlier. Power-resolved CL spectroscopy was performed by exposing a fixed area of sample (30 μm^2) with a constant accelerating voltage at 5 kV and varying the beam current from 0.1 to 3.2 nA.

For fs-TAS measurements, an integrated Helios and EOS setup (Ultrafast Systems LLC) was used and the measurements were performed at room temperature. Detailed descriptions of the instrument and the measurement techniques can be found elsewhere.[46] Briefly, a Ti:sapphire regenerative amplifier (Coherent Legend, 800 nm, 150 fs, 1 mJ) was used to generate 800 nm pulses, the frequency of which was doubled using a beta barium borate crystal to generate the 400 nm pump pulses. The probe pulses, which were white-light continuum, were generated by passing through a sapphire crystal. The pump beam was attenuated to 60 $\mu J/cm^2$, and the data were collected as a function of time delay between the pump and the probe pulses. For long-time scans (>ns), the white-light continuum was generated from a photonic fiber using a neodymium-doped yttrium aluminum garnet (Nd:YAG) laser (1064 nm).

The J–V curves of the devices were produced using a solar simulator (San-EI Electric, XEC 301S) at AM 1.5 illumination (a power density of 1000 $W \cdot m^{-2}$) and recorded by a Keithley model 2612A source meter. External quantum efficiency/IPCE measurement was carried out by PV300 (Bentham) equipped with a xenon/quartz halogen monochromatic light source.

ASSOCIATED CONTENT

Supporting Information

The Supporting Information is available free of charge on the ACS Publications website at DOI: 10.1021/acsami.7b14735.

Detailed PV performances of the $Cs_3Bi_2I_9$-based solar cell, thin-film morphology, PL spectroscopy, and time-resolved PL decay (PDF)

AUTHOR INFORMATION

Corresponding Author

*E-mail: nripan@ntu.edu.sg.

ORCID

Biplab Ghosh: 0000-0002-5584-1830

Tze Chien Sum: 0000-0003-4049-2719

Nripan Mathews: 0000-0001-5234-0822

Notes

The authors declare no competing financial interest.

ACKNOWLEDGMENTS

This research was supported by the National Research Foundation, Prime Minister's Office, Singapore under its Competitive Research Programme (CRP award no. NRF-CRP14-2014-03) and through the Singapore–Berkeley Research Initiative for Sustainable Energy (SinBeRISE) CREATE Program. T.C.S. would like to acknowledge the financial support from the Ministry of Education Academic Research Fund Tier 1 Grants RG101/15 and RG173/16 and Tier 2 Grants MOE2015-T2-2-015 and MOE2016-T2-1-034.

REFERENCES

(1) Gao, P.; Grätzel, M.; Nazeeruddin, M. K. Organohalide lead perovskites for photovoltaic applications. *Energy Environ. Sci.* **2014**, *7*, 2448–2463.

(2) Kojima, A.; Teshima, K.; Shirai, Y.; Miyasaka, T. Organometal Halide Perovskites as Visible-Light Sensitizers for Photovoltaic Cells. *J. Am. Chem. Soc.* **2009**, *131*, 6050–6051.

(3) Kim, H.-S.; Lee, C.-R.; Im, J.-H.; Lee, K.-B.; Moehl, T.; Marchioro, A.; Moon, S.-J.; Humphry-Baker, R.; Yum, J.-H.; Moser, J. E.; Grätzel, M.; Park, N.-G. Lead Iodide Perovskite Sensitized All-Solid-State Submicron Thin Film Mesoscopic Solar Cell with Efficiency Exceeding 9%. *Sci. Rep.* **2012**, *2*, 591.

(4) Park, N.-G. Organometal Perovskite Light Absorbers Toward a 20% Efficiency Low-Cost Solid-State Mesoscopic Solar Cell. *J. Phys. Chem. Lett.* **2013**, *4*, 2423–2429.

(5) Hao, F.; Stoumpos, C. C.; Cao, D. H.; Chang, R. P. H.; Kanatzidis, M. G. Lead-free solid-state organic-inorganic halide perovskite solar cells. *Nat. Photonics* **2014**, *8*, 489–494.

(6) Noel, N. K.; Stranks, S. D.; Abate, A.; Wehrenfennig, C.; Guarnera, S.; Haghighirad, A.-A.; Sadhanala, A.; Eperon, G. E.; Pathak, S. K.; Johnston, M. B.; Petrozza, A.; Herz, L. M.; Snaith, H. J. Lead-free organic-inorganic tin halide perovskites for photovoltaic applications. *Energy Environ. Sci.* **2014**, *7*, 3061–3068.

(7) Babayigit, A.; Thanh, D. D.; Ethirajan, A.; Manca, J.; Muller, M.; Boyen, H.-G.; Conings, B. Assessing the toxicity of Pb- and Sn-based perovskite solar cells in model organism Danio rerio. *Sci. Rep.* **2016**, *6*, 18721.

DOI: 10.1021/acsami.7b14735
ACS Appl. Mater. Interfaces XXXX, XXX, XXX–XXX

(8) Krishnamoorthy, T.; Ding, H.; Yan, C.; Leong, W. L.; Baikie, T.; Zhang, Z.; Sherburne, M.; Li, S.; Asta, M.; Mathews, N.; Mhaisalkar, S. G. Lead-free Germanium Iodide Perovskite Materials for Photovoltaic Applications. *J. Mater. Chem. A* **2015**, *3*, 23829−23832.
(9) Lehner, A. J.; Fabini, D. H.; Evans, H. A.; Hébert, C.-A.; Smock, S. R.; Hu, J.; Wang, H.; Zwanziger, J. W.; Chabinyc, M. L.; Seshadri, R. Crystal and Electronic Structures of Complex Bismuth Iodides $A_3Bi_2I_9$ (A = K, Rb, Cs) Related to Perovskite: Aiding the Rational Design of Photovoltaics. *Chem. Mater.* **2015**, *27*, 7137−7148.
(10) Shockley, W.; Queisser, H. J. Detailed Balance Limit of Efficiency of p-n Junction Solar Cells. *J. Appl. Phys.* **1961**, *32*, 510−519.
(11) Rühle, S. Tabulated values of the Shockley−Queisser limit for single junction solar cells. *Sol. Energy* **2016**, *130*, 139−147.
(12) Park, B.-W.; Philippe, B.; Zhang, X.; Rensmo, H.; Boschloo, G.; Johansson, E. M. J. Bismuth Based Hybrid Perovskites $A_3Bi_2I_9$ (A: Methylammonium or Cesium) for Solar Cell Application. *Adv. Mater.* **2015**, *27*, 6806−6813.
(13) Abulikemu, M.; Ould-Chikh, S.; Miao, X.; Alarousu, E.; Murali, B.; Ndjawa, G. O. N.; Barbé, J.; Labban, A. E.; Amassian, A.; Del Gobbo, S. Optoelectronic and photovoltaic properties of the air-stable organohalide semiconductor $(CH_3NH_3)_3Bi_2I_9$. *J. Mater. Chem. A* **2016**, *4*, 12504−12515.
(14) Singh, T.; Kulkarni, A.; Ikegami, M.; Miyasaka, T. Effect of Electron Transporting Layer on Bismuth-Based Lead-Free Perovskite $(CH_3NH_3)_3Bi_2I_9$ for Photovoltaic Applications. *ACS Appl. Mater. Interfaces* **2016**, *8*, 14542−14547.
(15) Lyu, M.; Yun, J.-H.; Cai, M.; Jiao, Y.; Bernhardt, P. V.; Zhang, M.; Wang, Q.; Du, A.; Wang, H.; Liu, G.; Wang, L. Organic−inorganic bismuth (III)-based material: A lead-free, air-stable and solution-processable light-absorber beyond organolead perovskites. *Nano Res.* **2016**, *9*, 692−702.
(16) Kawai, T.; Shimanuki, S. Optical Studies of $(CH_3NH_3)_3Bi_2I_9$ Single Crystals. *Phys. Status Solidi B* **1993**, *177*, K43−K45.
(17) Dammak, H.; Yangui, A.; Triki, S.; Abid, Y.; Feki, H. Structural characterization, vibrational, optical properties and DFT investigation of a new luminescent organic−inorganic material: (C6H14N)3Bi2I9. *J. Lumin.* **2015**, *161*, 214−220.
(18) Xing, G.; Mathews, N.; Sun, S.; Lim, S. S.; Lam, Y. M.; Gratzel, M.; Mhaisalkar, S.; Sum, T. C. Long-Range Balanced Electron- and Hole-Transport Lengths in Organic-Inorganic $CH_3NH_3PbI_3$. *Science* **2013**, *342*, 344−347.
(19) Johansson, M. B.; Zhu, H.; Johansson, E. M. J. Extended Photo-Conversion Spectrum in Low-Toxic Bismuth Halide Perovskite Solar Cells. *J. Phys. Chem. Lett.* **2016**, *7*, 3467−3471.
(20) Kumar, M. H.; Dharani, S.; Leong, W. L.; Boix, P. P.; Prabhakar, R. R.; Baikie, T.; Shi, C.; Ding, H.; Ramesh, R.; Asta, M.; Graetzel, M.; Mhaisalkar, S. G.; Mathews, N. Lead-Free Halide Perovskite Solar Cells with High Photocurrents Realized Through Vacancy Modulation. *Adv. Mater.* **2014**, *26*, 7122−7127.
(21) Liu, F.; Dong, Q.; Wong, M. K.; Djurišić, A. B.; Ng, A.; Ren, Z.; Shen, Q.; Surya, C.; Chan, W. K.; Wang, J.; Ng, A. M. C.; Liao, C.; Li, H.; Shih, K.; Wei, C.; Su, H.; Dai, J. Is Excess PbI2 Beneficial for Perovskite Solar Cell Performance? *Adv. Energy Mater.* **2016**, *6*, 1502206.
(22) Jacobsson, T. J.; Correa-Baena, J.-P.; Anaraki, E. H.; Philippe, B.; Stranks, S. D.; Bouduban, M. E. F.; Tress, W.; Schenk, K.; Teuscher, J.; Moser, J.-E.; Rensmo, H.; Hagfeldt, A. Unreacted PbI_2 as a Double-Edged Sword for Enhancing the Performance of Perovskite Solar Cells. *J. Am. Chem. Soc.* **2016**, *138*, 10331−10343.
(23) Ghosh, B.; Chakraborty, S.; Wei, H.; Guet, C.; Li, S.; Mhaisalkar, S.; Mathews, N. Poor Photovoltaic Performance of $Cs_3Bi_2I_9$: An Insight through First-Principles Calculations. *J. Phys. Chem. C* **2017**, *121*, 17062−17067.
(24) Miller, O. D.; Yablonovitch, E.; Kurtz, S. R. Strong Internal and External Luminescence as Solar Cells Approach the Shockley-Queisser Limit. *IEEE J. Photovolt.* **2012**, *2*, 303−311.
(25) McCall, K. M.; Stoumpos, C. C.; Kostina, S. S.; Kanatzidis, M. G.; Wessels, B. W. Strong Electron−Phonon Coupling and Self-Trapped Excitons in the Defect Halide Perovskites $A_3M_2I_9$ (A = Cs, Rb; M = Bi, Sb). *Chem. Mater.* **2017**, *29*, 4129−4145.
(26) Yacobi, B. G.; Holt, D. B. Cathodoluminescence. *Cathodoluminescence Microscopy of Inorganic Solids*; Springer US: Boston, MA, 1990; pp 55−88.
(27) Schmidt, T.; Lischka, K.; Zulehner, W. Excitation-power dependence of the near-band-edge photoluminescence of semiconductors. *Phys. Rev. B: Condens. Matter Mater. Phys.* **1992**, *45*, 8989−8994.
(28) Reshchikov, M. A.; Korotkov, R. Y. Analysis of the temperature and excitation intensity dependencies of photoluminescence in undoped GaN films. *Phys. Rev. B: Condens. Matter Mater. Phys.* **2001**, *64*, 115205.
(29) Singh, R.; Molnar, R. J.; Ünlü, M. S.; Moustakas, T. D. Intensity dependence of photoluminescence in GaN thin films. *Appl. Phys. Lett.* **1994**, *64*, 336−338.
(30) Rezgui, B. D.; Veirman, J.; Dubois, S.; Palais, O. Study of donor−acceptor pair luminescence in highly doped and compensated Cz silicon. *Phys. Status Solidi A* **2012**, *209*, 1917−1920.
(31) Shi, H.; Yan, R.; Bertolazzi, S.; Brivio, J.; Gao, B.; Kis, A.; Jena, D.; Xing, H. G.; Huang, L. Exciton Dynamics in Suspended Monolayer and Few-Layer MoS_2 2D Crystals. *ACS Nano* **2013**, *7*, 1072−1080.
(32) Wu, X.; Trinh, M. T.; Zhu, X.-Y. Excitonic Many-Body Interactions in Two-Dimensional Lead Iodide Perovskite Quantum Wells. *J. Phys. Chem. C* **2015**, *119*, 14714−14721.
(33) Cui, Q.; Ceballos, F.; Kumar, N.; Zhao, H. Transient Absorption Microscopy of Monolayer and Bulk WSe_2. *ACS Nano* **2014**, *8*, 2970−2976.
(34) Sim, S.; Park, J.; Song, J.-G.; In, C.; Lee, Y.-S.; Kim, H.; Choi, H. Exciton dynamics in atomically thin MoS_2: Interexcitonic interaction and broadening kinetics. *Phys. Rev. B: Condens. Matter Mater. Phys.* **2013**, *88*, 075434.
(35) Scholz, M.; Flender, O.; Oum, K.; Lenzer, T. Pronounced Exciton Dynamics in the Vacancy-Ordered Bismuth Halide Perovskite $(CH_3NH_3)_3Bi_2I_9$ Observed by Ultrafast UV−vis−NIR Transient Absorption Spectroscopy. *J. Phys. Chem. C* **2017**, *121*, 12110−12116.
(36) Ponseca, C. S.; Savenije, T. J.; Abdellah, M.; Zheng, K.; Yartsev, A.; Pascher, T.; Harlang, T.; Chabera, P.; Pullerits, T.; Stepanov, A.; Wolf, J.-P.; Sundström, V. Organometal Halide Perovskite Solar Cell Materials Rationalized: Ultrafast Charge Generation, High and Microsecond-Long Balanced Mobilities, and Slow Recombination. *J. Am. Chem. Soc.* **2014**, *136*, 5189−5192.
(37) Yin, J.; Cortecchia, D.; Krishna, A.; Chen, S.; Mathews, N.; Grimsdale, A. C.; Soci, C. Interfacial Charge Transfer Anisotropy in Polycrystalline Lead Iodide Perovskite Films. *J. Phys. Chem. Lett.* **2015**, *6*, 1396−1402.
(38) Kapil, G.; Ohta, T.; Koyanagi, T.; Vigneshwaran, M.; Zhang, Y.; Ogomi, Y.; Pandey, S. S.; Yoshino, K.; Shen, Q.; Toyoda, T.; Rahman, M. M.; Minemoto, T.; Murakami, T. N.; Segawa, H.; Hayase, S. Investigation of Interfacial Charge Transfer in Solution Processed Cs_2SnI_6 Thin Films. *J. Phys. Chem. C* **2017**, *121*, 13092−13100.
(39) Harikesh, P. C.; Mulmudi, H. K.; Ghosh, B.; Goh, T. W.; Teng, Y. T.; Thirumal, K.; Lockrey, M.; Weber, K.; Koh, T. M.; Li, S.; Mhaisalkar, S.; Mathews, N. Rb as an Alternative Cation for Templating Inorganic Lead-Free Perovskites for Solution Processed Photovoltaics. *Chem. Mater.* **2016**, *28*, 7496−7504.
(40) Volonakis, G.; Haghighirad, A. A.; Milot, R. L.; Sio, W. H.; Filip, M. R.; Wenger, B.; Johnston, M. B.; Herz, L. M.; Snaith, H. J.; Giustino, F. $Cs_2InAgCl_6$: A New Lead-Free Halide Double Perovskite with Direct Band Gap. *J. Phys. Chem. Lett.* **2017**, *8*, 772−778.
(41) Greul, E.; Petrus, M. L.; Binek, A.; Docampo, P.; Bein, T. Highly stable, phase pure $Cs_2AgBiBr_6$ double perovskite thin films for optoelectronic applications. *J. Mater. Chem. A* **2017**, *5*, 19972−19981.
(42) Xiao, Z.; Du, K.-Z.; Meng, W.; Wang, J.; Mitzi, D. B.; Yan, Y. Intrinsic Instability of $Cs_2In(I)M(III)X6$ (M = Bi, Sb; X = Halogen) Double Perovskites: A Combined Density Functional Theory and Experimental Study. *J. Am. Chem. Soc.* **2017**, *139*, 6054−6057.
(43) Zhao, X.-G.; Yang, J.-H.; Fu, Y.; Yang, D.; Xu, Q.; Yu, L.; Wei, S.-H.; Zhang, L. Design of Lead-Free Inorganic Halide Perovskites for

DOI: 10.1021/acsami.7b14735
ACS Appl. Mater. Interfaces XXXX, XXX, XXX−XXX

654 Solar Cells via Cation-Transmutation. *J. Am. Chem. Soc.* **2017**, *139*,
655 2630−2638.
656 (44) Turkevych, I.; Kazaoui, S.; Ito, E.; Urano, T.; Yamada, K.;
657 Tomiyasu, H.; Yamagishi, H.; Kondo, M.; Aramaki, S. Photovoltaic
658 Rudorffites: Lead-Free Silver Bismuth Halides Alternative to Hybrid
659 Lead Halide Perovskites. *ChemSusChem* **2017**, *10*, 3754−3759.
660 (45) Ni, C.; Hedley, G.; Payne, J.; Svrcek, V.; McDonald, C.;
661 Jagadamma, L. K.; Edwards, P.; Martin, R.; Jain, G.; Carolan, D.;
662 Mariotti, D.; Maguire, P.; Samuel, I.; Irvine, J. Charge carrier localised
663 in zero-dimensional $(CH_3NH_3)_3Bi_2I_9$ clusters. *Nat. Commun.* **2017**, *8*,
664 170.
665 (46) Wu, B.; Nguyen, H. T.; Ku, Z.; Han, G.; Giovanni, D.; Mathews,
666 N.; Fan, H. J.; Sum, T. C. Discerning the Surface and Bulk
667 Recombination Kinetics of Organic-Inorganic Halide Perovskite Single
668 Crystals. *Adv. Energy Mater.* **2016**, *6*, 1600551.

DOI: 10.1021/acsami.7b14735
ACS Appl. Mater. Interfaces XXXX, XXX, XXX−XXX